

# Efficient qutrit gate-set tomography on a transmon

Shuxiang Cao,<sup>1,\*</sup> Deep Lall,<sup>2,3</sup> Mustafa Bakr,<sup>1</sup> Giulio Campanaro,<sup>1</sup> Simone Fasciati,<sup>1</sup> James Wills,<sup>1</sup> Vivek Chidambaram,<sup>1</sup> Boris Shteynas,<sup>1</sup> Ivan Rungger,<sup>2</sup> and Peter Leek<sup>1,†</sup>

<sup>1</sup>*Department of Physics, Clarendon Laboratory, University of Oxford, OX1 3PU, UK*

<sup>2</sup>*National Physical Laboratory, Teddington, TW11 0LW, UK*

<sup>3</sup>*Department of Materials, University of Oxford, Parks Road, Oxford, OX1 3PH, UK*

Gate-set tomography enables the determination of the process matrix of a set of quantum logic gates, including measurement and state preparation errors. Here we propose an efficient method to implement such tomography on qutrits, using only gates in the qutrit Clifford group to construct preparation and measurement fiducials. Our method significantly reduces computational overhead by using the theoretical minimum number of measurements and directly parametrizing qutrit Hadamard gates. We demonstrate qutrit gate-set tomography on a superconducting transmon, and find good agreement of average gate infidelity with qutrit randomized benchmarking.

*Introduction* Quantum computation (QC) is fundamentally different from classical computing due to the exponentially large computation space that can be accessed [1–4]. Although QC is traditionally based on 2-level quantum systems (qubits), extending to  $d$ -level systems (qudits) ( $d > 2$ ) can potentially overcome technical challenges with current QC schemes: it can reduce the number of elementary units of a physical device [5–8], improve computation efficiency [7, 9–11] and simplify the implementation of quantum gates [12, 13]. A natural candidate for implementing a qudit is the transmon, a non-linear superconducting resonator built from a capacitively-shunted Josephson junction [14]. Using a superconducting transmon as a qutrit is an emerging research direction, with recent demonstrations of novel quantum state control [15–19], quantum metrology [20] and quantum simulation [21, 22].

To build a qudit-based quantum processor, compatible tools for characterizing the performance of its qudit logic gates become essential. Randomized benchmarking (RB) is widely used to extract the average gate infidelity [23, 24], and recently has been demonstrated on a superconducting qutrit [25, 26]. RB can extract the average gate fidelity of a specific gate, however it cannot provide information on the detailed nature of the errors. It is critical to understand these details in order to eliminate the errors [27], and to implement quantum error mitigation [28, 29].

Any quantum process can be described using the process matrix, and the standard method to characterize this matrix is process tomography [30]. Process tomography is a protocol to reconstruct the quantum process of the specific gate, with the assumption that the state preparation and measurement (SPAM) error is negligible. As an improvement on this method, gate-set tomography (GST) [31, 32] takes the influence of SPAM errors into account; it performs process tomography for all gates in the gate set including all the elementary gates for state

preparation and measurement. Then an estimation for the gate process can be approximated by optimizing the process matrix and SPAM operators with the information of the entire gate set. GST has been used to characterise quantum processes in superconducting qubits [33–35], ion traps [27], nuclear spin qubits [36], and has also been used to perform time-domain tracking to analyze the parameter drift problem for quantum control [37, 38].

In this letter, we propose and demonstrate an efficient gate-set tomography method for characterization of transmon qutrits. Our method uses only qutrit Clifford gates for state preparation and measurement in different bases. The proposed tomography method reduces the computational cost in the following ways. First, the measurement basis is chosen so that it needs the theoretical minimum number of measurements to implement qutrit tomography. Secondly, instead of parameterizing all the physical gates in the gate set, our method directly parameterizes the qutrit Hadamard gate, which occurs frequently when synthesising qutrit Clifford gates. Such configuration reduces the computation cost for the GST optimization process. We implement this method on a superconducting transmon and extract the full process matrices and SPAM errors. The GST reported average gate infidelity is in good agreement with that obtained by qutrit randomized benchmarking (RB).

*Physical device* The qutrit characterized in this letter is a single superconducting transmon implemented in a 3D-integrated coaxial circuit design [39, 40]. A transmon is a multilevel quantum Duffing oscillator consisting of a Josephson junction and a shunting capacitance [14]. The basic device parameters are given in appendix A. We utilize the first three transmon energy levels as our qutrit, labelling them as  $|n\rangle$ , where  $n = 0, 1, 2$ , see Figure. 1.

We employ as physical gates the same ones that would be used for single qubit gates on the  $\{|0\rangle, |1\rangle\}$  and  $\{|1\rangle, |2\rangle\}$  subspaces, which corresponds to driving transitions between adjacent energy levels. The qutrit virtual Z gate is included to complete a universal gate set; it is an extension of the qubit virtual Z gate [41] implemented by shifting the phase of the subsequent pulses.

The tomography method requires implementing qutrit

\* shuxiang.cao@physics.ox.ac.uk

† peter.leek@physics.ox.ac.uk

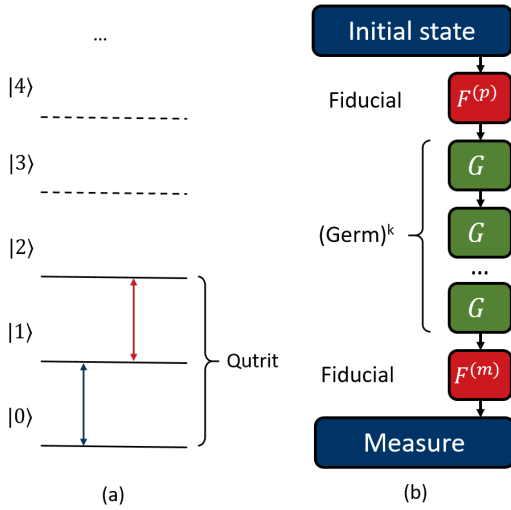


FIG. 1. (a) The experiment is implemented on a transmon with the first 3 levels as computational space. The physical gates are implemented on  $\{|0\rangle, |1\rangle\}$  and  $\{|1\rangle, |2\rangle\}$  subspace. The 4th level is used to characterize the leakage error. (b) Gate sequence to collect data  $m_{ijkl}$  for gate set tomography. The fiducial gates are used to prepare the initial states and the measurement basis. The germs are gate sequences composed of gates in the gate set, which can boost the errors of single gates in the gate set.

Clifford gates, which can be synthesised by  $H$  and virtual  $Z$  gates.  $H$  is implemented with the following sequence of gates [25]:

$$H = H_{12}Z_1(\pi)Z_2(\pi)Y_{01}(\theta_m)H_{12}, \quad (1)$$

where  $\theta_m = 2 \arccos(1/\sqrt{3})$  is the magic angle [42], and  $Y_{01}(\theta_m)$  is implemented with a single pulse modulating the amplitude. The virtual gates  $Z_1(\theta)$  and  $Z_2(\theta)$  add phases on the  $|1\rangle$  and  $|2\rangle$  states, respectively.  $H_{12}$  is the Hadamard gate in the  $\{|1\rangle, |2\rangle\}$  subspace, which is synthesised by  $H_{12} = Y_{12}(\pi/2)Z_2(\pi)$ , where  $Y_{ij}(\theta)$  is the Pauli  $Y$  rotation with rotation angle  $\theta$  applied to the  $\{|i\rangle, |j\rangle\}$  subspace.

*Gate set tomography* The goal of gate set tomography is to reconstruct the quantum process of all the gates in the gate set,  $\mathcal{G}$ , taking into account that the initial state preparation and measurements are imperfect. The following discussion utilizes the superoperator formalism [43], representing the density operator  $\rho$  and measurement operator  $E$  as a vector in Schmidt-Hilbert space, denoted by superket  $|\rho\rangle\rangle$  and super bra  $\langle\langle E|$ , respectively. See appendix B for more details. In this letter we perform maximum likelihood GST [31, 44], which collects the following data from the measured probability distributions:

$$m_{ijkl} = \langle\langle E_l | F_i^{(m)} G_k F_j^{(p)} | \rho_0 \rangle\rangle, \quad (2)$$

where  $|\rho_0\rangle\rangle$  is the initial state and  $\langle\langle E_l |$  is the measurement basis that can be directly implemented on the hard-

ware. The fiducials  $F_j^{(p)}$  represent the quantum processes for preparing the initial states, and  $F_i^{(m)}$  for implementing measurement basis. Sandwiched between the fiducials,  $G_k \in \mathcal{G}$  is the quantum process in the gate set, which contains all the gates we are interested in, and the gates use to implement  $F_i^{(m)}$  and  $F_j^{(p)}$ . To make the GST more accurate,  $G_k$  is usually replaced with a gate sequence that amplifies the coherent error, known as a sequence of germs [45]. Once the gate-set is defined, the germs we use in this work are calculated from the PyGSTi [45] germs generation routine. The estimated quantum processes  $\tilde{G}_k$  for all  $G_k$  can be found with the maximum likelihood method by minimizing the objective function

$$\begin{aligned} \mathcal{L}_m(\tilde{E}_l, \tilde{F}_i^{(m)}, \tilde{G}_k, \tilde{F}_j^{(p)}, \rho) \\ = \sum_{ijkl} (\langle\langle \tilde{E}_l | \tilde{F}_i^{(m)} \tilde{G}_k \tilde{F}_j^{(p)} | \rho \rangle\rangle - m_{ijkl})^2 \end{aligned} \quad (3)$$

where  $\tilde{E}_l$ ,  $\tilde{F}_i^{(m)}$ ,  $\tilde{G}_k$ ,  $\tilde{F}_j^{(p)}$ ,  $\tilde{\rho}_0$  are the estimated value for the physical operators  $E_l$ ,  $F_i^{(m)}$ ,  $G_k$ ,  $F_j^{(p)}$ ,  $\rho_0$ . Minimizing this objective function is an optimisation problem that is subject to a number of constraints, which ensure that all the estimated operators are physical [45].

Such optimization is usually computationally expensive. Firstly, the number of free parameters that need to be optimized is proportional to the number of gates in the gate-set used to synthesise the fiducials and germs. The optimizer for fitting the experimental data, for example, the Levenberg-Marquardt Algorithm [46] used by PyGSTi, requires the evaluation of the Jacobian matrix at each optimization step. The size of the Jacobian matrix is proportional to the number of free parameters and the number of elements of  $m_{ijkl}$ . The computation cost of evaluating the Jacobian matrix is proportional to the length of the gate sequence [32]. Similar arguments are applied to the Hessian matrix for error bar estimation, which has a size proportional to the square of free parameters and size of  $m_{ijkl}$  [32] and hence even worse scaling. Also, collecting  $m_{ijkl}$  from experiments can be time-consuming. It would therefore be best if we could minimize the size of  $m_{ijkl}$ , shorten the gate sequence, and reduce the number of different gates involved in synthesizing all fiducials.

We therefore introduce two methods to reduce computational costs for GST. First, we choose a measurement basis that can be prepared with gates in the qutrit Clifford group shown in Table II. While previous physical proposals for tomography use an over-complete basis with 9 measurements [47, 48], our proposal requires only 4. In experiment we use standard dispersive measurement that can distinguish 3 different states with a single shot, and determine 2 degrees of freedom of the qutrit density matrix [49]. Since a qutrit density matrix has a total of 8 degrees of freedom, we require a minimum of 4 such measurements to implement qutrit state tomography.

TABLE I. The gate set and the set of germs chosen for gate set tomography of this experiment.

Gate set, $\mathcal{G}$		
$I$	$H$	$X_{01}(\frac{\pi}{2})$
$X_{12}(\frac{\pi}{2})$	$Z_1(\frac{2\pi}{3})$	$Z_2(\frac{2\pi}{3})$
List of germs, $G_k$		
$I$	$H$	$X_{01}(\frac{\pi}{2})$
$X_{12}(\frac{\pi}{2})$	$Z_1(\frac{2\pi}{3})$	$Z_2(\frac{2\pi}{3})$
$X_{01}(\frac{\pi}{2})X_{12}(\frac{\pi}{2})$	$H.Z_1(\frac{2\pi}{3})$	$H.Z_2(\frac{2\pi}{3})$
$H.X_{01}(\frac{\pi}{2})$	$X_{12}(\frac{\pi}{2}).Z_2(\frac{2\pi}{3})$	$X_{12}(\frac{\pi}{2}).Z_1(\frac{2\pi}{3})$
$H.X_{12}(\frac{\pi}{2})$	$X_{01}(\frac{\pi}{2}).Z_1(\frac{2\pi}{3})$	

TABLE II. Fiducials for qutrit gate set tomography.

Preparation Fiducials ( $F^{(p)}$ )	
1	$I$
2	$H.H.H.Z_2(\frac{2\pi}{3}).H$
3	$H.H.H.Z_1(\frac{2\pi}{3}).Z_2(\frac{2\pi}{3}).Z_2(\frac{2\pi}{3}).H$
4	$H.H.H.Z_1(\frac{2\pi}{3}).Z_1(\frac{2\pi}{3}).Z_2(\frac{2\pi}{3}).H$
5	$H.H.H.Z_1(\frac{2\pi}{3}).Z_2(\frac{2\pi}{3}).H$
6	$H.H.H.Z_1(\frac{2\pi}{3}).Z_1(\frac{2\pi}{3}).H$
7	$H.H.H.Z_1(\frac{2\pi}{3}).Z_1(\frac{2\pi}{3}).Z_2(\frac{2\pi}{3}).Z_2(\frac{2\pi}{3}).H$
8	$H.H.H.Z_2(\frac{2\pi}{3}).H.Z_2(\frac{2\pi}{3})$
9	$H.H.H.Z_1(\frac{2\pi}{3}).Z_1(\frac{2\pi}{3}).Z_2(\frac{2\pi}{3}).Z_2(\frac{2\pi}{3}).H.Z_2(\frac{2\pi}{3})$
Measurement Fiducials ( $F^{(m)}$ )	
1	$I$
2	$Z_2(\frac{2\pi}{3}).H.H.H.Z_2(\frac{2\pi}{3}).H$
3	$H.H.H.Z_1(\frac{2\pi}{3}).Z_2(\frac{2\pi}{3}).H$
4	$H.H.H.Z_2(\frac{2\pi}{3}).H$

The second method to reduce the computational cost is directly parameterizing  $H$  itself in the gate set, instead of the physical gates from which we synthesise it. The brute-force approach would parameterize  $Y_{01}(m)$  and replace  $H$  with a sequence of 5 gates (see Equation 1).  $H$  frequently occurs during the fiducial synthesis; directly parameterizing the  $H$  shortens the gate sequence and reduces the required computation cost.

Since all fiducials are in the qutrit Clifford group, only virtual- $Z$  gates and Hadamard gates are required to implement all the fiducials. The computational cost can be further reduced if we make the reasonable assumption that all virtual- $Z$  gates are perfect. Since we still want to directly characterize the physical gates  $X_{01}(\pi/2)$  and  $X_{12}(\pi/2)$ , we add them to the gate set, but do not include them for fiducial synthesis. This implies that  $H$  is independent of  $X_{01}(\pi/2)$  and  $X_{12}(\pi/2)$ , and ignores some information to more precisely characterize the  $X_{01}(\pi/2)$  and  $X_{12}(\pi/2)$ . Our experimental results show that under such configuration our qutrit GST produces an accurate estimation of the quantum process.

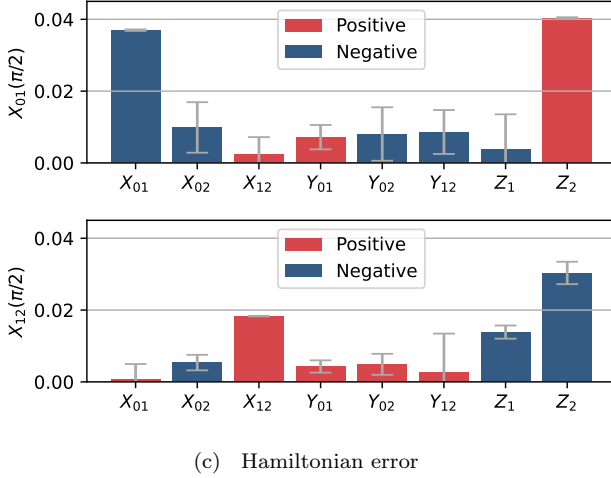
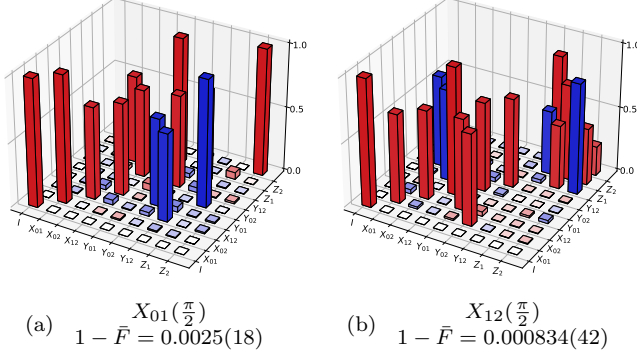
We now proceed and implement the GST on the superconducting transmon qutrit. The maximum sequence length is 512 germs, and we repeat sampling each sequence 500 times. The collected data is then processed by

the PyGSTi software with a customized model with the gate set and fiducials configuration as described above. The SPAM error characterized by the reconstructed initial state density matrix and the measurement operators are reported in Figure 3. The reconstructed process matrices for  $X_{01}(\pi/2)$ ,  $X_{12}(\pi/2)$  are shown in Figures 2a and 2b. The unitary average infidelity is reported in Table 2d. Since  $H$  occurs frequently in synthesizing fiducials, it is estimated more precisely and has a lower error bar than  $X_{01}(\pi/2)$  and  $X_{12}(\pi/2)$ . Note that the infidelities of the virtual- $Z$  gates are two orders of magnitude lower than those of physical gates, indicating that our assumption of perfect virtual- $Z$  gates is a valid approximation.

The advantage of GST compared to RB is that it provides a better characterization of the detailed nature of the errors. We use *error generators* [50] to facilitate this characterization. Consider the ideal target map  $\hat{G}_i$  for a physical reconstructed map  $G_i$ , the post-gate error generator  $L_i$  is defined as  $G_i = e^{L_i}\hat{G}_i$ . The error generator  $L$  can be further decomposed as  $L = L_H + L_S + L_A + L_C$ , a summation of coherent ( $L_H$ ), stochastic ( $L_S, L_C$ ) and active ( $L_A$ ) projected error generators, and hence quantify the contribution of different error sources [50]. Here we find coherent errors to be dominant for both  $X_{01}(\pi/2)$  (99.1(15)%) and  $X_{12}(\pi/2)$  (99.9(14)%). The components of  $L_H$  are shown in Figure 3c. Apart from the over or under rotation error ( $X_{01}$  and  $X_{12}$ ), the  $Z_2$  error, which denotes the frequency shift of the  $|2\rangle$  state, also contributes a significant amount of coherent error. This may be caused by AC Stark shifts on the  $|2\rangle$  state under driving. *Qutrit randomized benchmarking* We implement qutrit Clifford RB [23–25] to characterize the averaged gate fidelity and compare it with the GST result. RB fits the success probability  $P(|0\rangle)$  with a form  $Ap^m + B$ , where  $A$ ,  $B$  and  $p$  are fitting parameters, and  $m$  is the number of Clifford gates. The average error per Clifford is given by  $r = (1-p)(d-1)/d$ , where  $d = 2$  for qubits and  $d = 3$  for qutrits. The average error per physical gate for qubit-like RB is  $(1 - r^{1/N_g})(d-1)/d$ , where  $N_g = 1.825$  is the average number of physical gates required to implement a Clifford gate in this experiment.

The qutrit Clifford gates are synthesized with only the qutrit Hadamard gate  $H$  and the virtual  $Z$  gates. We implement single-qubit Clifford group RB on two-level subspaces  $\{|0\rangle, |1\rangle\}$  and  $\{|1\rangle, |2\rangle\}$ . Then we implement both standard qutrit Clifford RB and interleaved qutrit RB on the qutrit Hadamard gate [25, 51]. The qutrit Hadamard gate fidelity can be estimated by  $r_H = (1-p_i/p)(d-1)/d$ , where  $p_i$  is the exponential fitting parameter from the interleaved qutrit RB, and  $p$  is the parameter from standard qutrit RB.

We report the result from randomized benchmarking in the Table 4(e). We find the average gate infidelity obtained from RB to be in reasonable agreement with our GST results. Both GST and RB report a lower fidelity for the  $\{|0\rangle, |1\rangle\}$  than the  $\{|1\rangle, |2\rangle\}$  subspace. This is likely due to the choice of LO signal frequency closer to



Parameter	Value $\times 10^3$
Average $I$ gate infidelity	0.556(75)
Average $Z_1(\frac{2\pi}{3})$ gate infidelity	0.0348(89)
Average $Z_2(\frac{2\pi}{3})$ gate infidelity	0.011(61)
Average $X_{01}(\frac{\pi}{2})$ gate infidelity	3.28(23)
Average $X_{12}(\frac{\pi}{2})$ gate infidelity	1.112(56)
Qutrit Hadamard Gate infidelity	2.97(12)

(d) Parameter summary

FIG. 2. (a) Estimated process matrix for  $X_{01}(\frac{\pi}{2})$  and (b) for  $X_{12}(\frac{\pi}{2})$ . See appendix B for more details. (c) Projected Hamiltonian error generator of the quantum logic gate, showing the strength of different coherent errors. See appendix C for more details. The error bar is generated from the Hessian projection method provided in the pyGSTi package, with the confidence level set to 95%.

the transition frequency between  $\{|1\rangle, |2\rangle\}$ , see appendix A.

*Conclusion* We have demonstrated using gate set tomography to characterize a single superconducting qutrit. The fiducials are synthesized with only the qutrit Hadamard gate and qutrit virtual Z gate to speed up the optimization process of gate-set tomography. We also choose an efficient measurement basis to use the minimum measurement number to implement tomography.

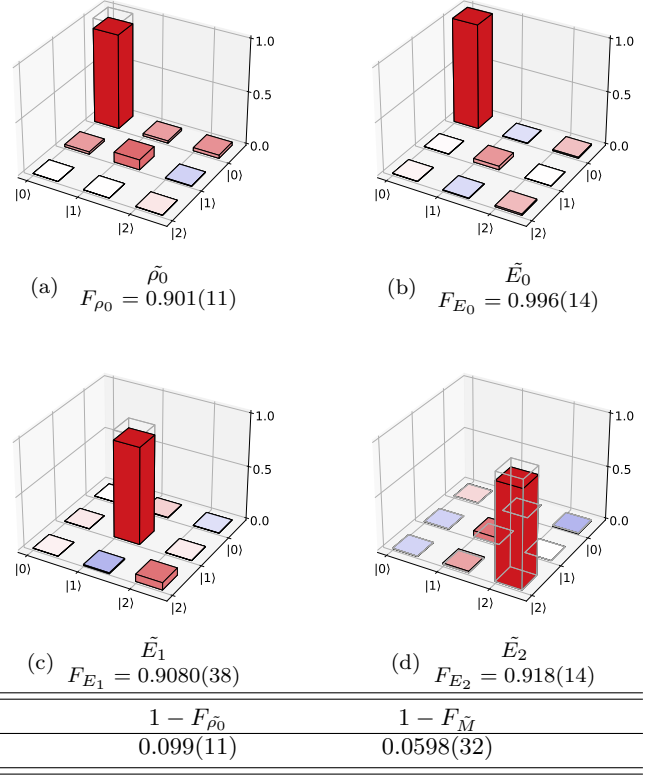
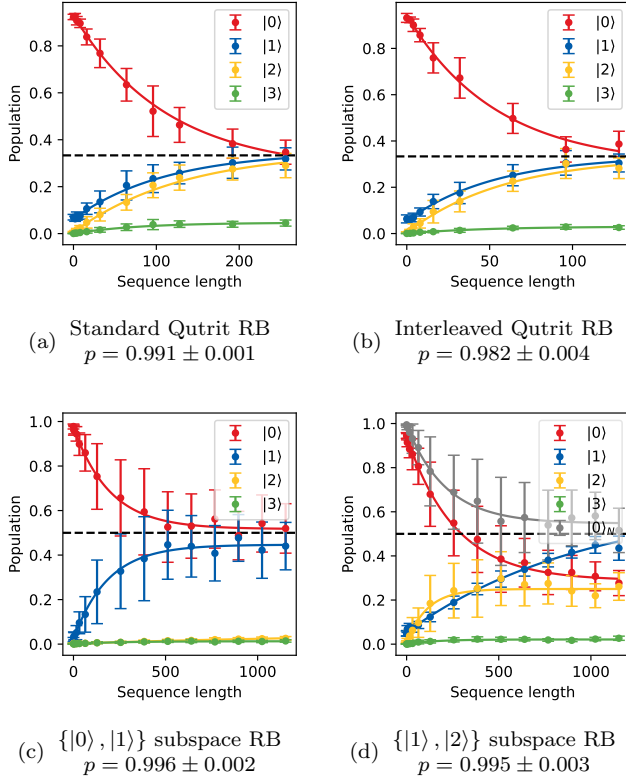


FIG. 3. Characterization of SPAM errors: (a) estimated initial state density matrix; (b) to (d) Estimated measurement operator  $\tilde{E}_i$  for state set to  $|i\rangle$ .  $F_{\rho_0}$  and  $F_{\bar{M}}$  denote the initial state fidelity and the averaged measurement fidelity. The error bar indicates 95% confidence level.

The above configuration significantly reduces the computation costs. The GST results shows the coherent error is dominant for the physical gates, and the virtual Z gates have infidelity two orders of magnitude lower than the physical gates. We compare the GST result with the randomized benchmarking result and confirm the correctness of GST. We conclude that our proposed GST method is correct, efficient and effective.

## ACKNOWLEDGMENTS

P.L. acknowledges support from the EPSRC [EP/T001062/1, EP/N015118/1, EP/M013243/1]. D.L. and I.R. acknowledge the support of the UK government department for Business, Energy and Industrial Strategy through the UK National Quantum Technologies Programme. We thank Heng Shen, Yutian Wen, Xianxin Guo for insightful discussions. We acknowledge the use of the University of Oxford Advanced Research Computing facility.



Parameter	Value $\times 10^3$
$\{ 0\rangle,  1\rangle\}$ Clifford gate infidelity	1.9(19)
$\{ 0\rangle,  1\rangle\}$ physical gate infidelity	1.1(11)
$\{ 1\rangle,  2\rangle\}$ Clifford gate infidelity	2.4(22)
$\{ 1\rangle,  2\rangle\}$ physical gate infidelity	1.3(12)
Average Qutrit Clifford infidelity	5.93(15)
Hadamard gate infidelity	6.3(48)
$\{ 0\rangle,  1\rangle\}$ leakage per qubit-like Clifford gate	0.63(19)
$\{ 1\rangle,  2\rangle\}$ leakage per qubit-like Clifford gate	0.16(11)
Leakage per qutrit Clifford gate	0.669(22)

(e) Parameter summary

FIG. 4. Randomized benchmarking (RB) results. Here 4-level single-shot measurement is used to distinguish 4 states. The error bar for  $p$  parameter indicates one standard deviation of uncertainty. (a) Standard RB on the qutrit Clifford gate set. (b) Interleaved RB on the qutrit Hadamard gate. (c) Qubit-like RB for the  $\{|0\rangle, |1\rangle\}$  subspace. (d) Qubit-like RB for the  $\{|1\rangle, |2\rangle\}$  subspace. The qutrit population in  $|1\rangle$  is swapped with  $|0\rangle$  at the end of each sequence.  $|0\rangle_N$  is the renormalized population of  $|0\rangle$ , where the population of the  $|1\rangle$  and  $|3\rangle$  states is excluded. (e) Infidelity obtained from RB experiments. The error bar in this table indicates 95% confidence interval.

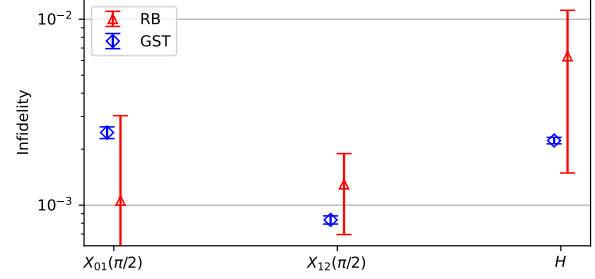


FIG. 5. Comparison between GST results and the RB results. The size of the error bar indicates 95% confidence interval. The blue and red color represent the GST results and the RB results respectively.

- 
- [1] M. A. Nielsen and I. L. Chuang, *Quantum Computation and Quantum Information: 10th Anniversary Edition* (Cambridge University Press, 2011).
- [2] X. Yuan, A quantum-computing advantage for chemistry, *Science* **369**, 1054 (2020).
- [3] D. Risté, M. P. da Silva, C. A. Ryan, A. W. Cross, A. D. Córcoles, J. A. Smolin, J. M. Gambetta, J. M. Chow, and B. R. Johnson, Demonstration of quantum advantage in machine learning, *npj Quantum Information* **3**, 16 (2017).
- [4] A. Steane, Quantum computing, *Reports on Progress in Physics* **61**, 117 (1998).
- [5] A. Muthukrishnan and C. R. Stroud, Multivalued logic gates for quantum computation, *Phys. Rev. A* **62**, 052309 (2000).
- [6] P. Gokhale, J. M. Baker, C. Duckering, F. T. Chong, N. C. Brown, and K. R. Brown, Extending the frontier of quantum computers with qutrits, *IEEE Micro* **40**, 64 (2020).
- [7] Y. Wang, Z. Hu, B. C. Sanders, and S. Kais, Qudits and high-dimensional quantum computing, *Frontiers in Physics* **8**, 10.3389/fphy.2020.589504 (2020).
- [8] A. Bocharov, M. Roetteler, and K. M. Svore, Factoring with qutrits: Shor’s algorithm on ternary and meta-plectic quantum architectures, *Phys. Rev. A* **96**, 012306 (2017).
- [9] D. P. O’Leary, G. K. Brennen, and S. S. Bullock, Parallelism for quantum computation with qudits, *Phys. Rev. A* **74**, 032334 (2006).
- [10] Y.-M. Di and H.-R. Wei, Synthesis of multivalued quantum logic circuits by elementary gates, *Phys. Rev. A* **87**, 012325 (2013).
- [11] B. Li, Z.-H. Yu, and S.-M. Fei, Geometry of quantum computation with qutrits, *Scientific Reports* **3**, 2594 (2013).
- [12] B. P. Lanyon, M. Barbieri, M. P. Almeida, T. Jennewein, T. C. Ralph, K. J. Resch, G. J. Pryde, J. L. O’Brien, A. Gilchrist, and A. G. White, Simplifying quantum logic using higher-dimensional hilbert spaces, *Nature Physics* **5**, 134 (2009).
- [13] A. S. Nikolaeva, E. O. Kiktenko, and A. K. Fedorov, Decomposing the generalized toffoli gate with qutrits, *Phys. Rev. A* **105**, 032621 (2022).
- [14] J. Koch, T. M. Yu, J. Gambetta, A. A. Houck, D. I. Schuster, J. Majer, A. Blais, M. H. Devoret, S. M. Girvin, and R. J. Schoelkopf, Charge-insensitive qubit design derived from the cooper pair box, *Phys. Rev. A* **76**, 042319 (2007).
- [15] S. Danilin, A. Vepsäläinen, and G. S. Paraoanu, Experimental state control by fast non-abelian holonomic gates with a superconducting qutrit, *Physica Scripta* **93**, 055101 (2018).
- [16] Y. Liu, D. Lan, X. Tan, J. Zhao, P. Zhao, M. Li, K. Zhang, K. Dai, Z. Li, Q. Liu, S. Huang, G. Xue, P. Xu, H. Yu, S.-L. Zhu, and Y. Yu, Realization of dark state in a three-dimensional transmon superconducting qutrit, *Applied Physics Letters* **107**, 202601 (2015).
- [17] A. Cervera-Lierta, M. Krenn, A. Aspuru-Guzik, and A. Galda, Experimental high-dimensional greenberger-horne-zeilinger entanglement with superconducting transmon qutrits, *Phys. Rev. Applied* **17**, 024062 (2022).
- [18] R.-Y. Yan, F. Yang, N. Zhang, and Z.-B. Feng, Accelerated and robust population transfer in a transmon qutrit via delta-type driving, *Quantum Information Processing* **17**, 237 (2018).
- [19] X.-J. Lu, M. Li, Z. Y. Zhao, C.-L. Zhang, H.-P. Han, Z.-B. Feng, and Y.-Q. Zhou, Nonleaky and accelerated population transfer in a transmon qutrit, *Phys. Rev. A* **96**, 023843 (2017).
- [20] A. R. Shlyakhov, V. V. Zemlyanov, M. V. Suslov, A. V. Lebedev, G. S. Paraoanu, G. B. Lesovik, and G. Blatter, Quantum metrology with a transmon qutrit, *Phys. Rev. A* **97**, 022115 (2018).
- [21] X. Tan, D.-W. Zhang, Q. Liu, G. Xue, H.-F. Yu, Y.-Q. Zhu, H. Yan, S.-L. Zhu, and Y. Yu, Topological maxwell metal bands in a superconducting qutrit, *Phys. Rev. Lett.* **120**, 130503 (2018).
- [22] M. S. Blok, V. V. Ramasesh, T. Schuster, K. O’Brien, J. M. Kreikebaum, D. Dahlen, A. Morvan, B. Yoshida, N. Y. Yao, and I. Siddiqi, Quantum information scrambling on a superconducting qutrit processor, *Phys. Rev. X* **11**, 021010 (2021).
- [23] C. Dankert, R. Cleve, J. Emerson, and E. Livine, Exact and approximate unitary 2-designs and their application to fidelity estimation, *Phys. Rev. A* **80**, 012304 (2009).
- [24] J. Emerson, R. Alicki, and K. Życzkowski, Scalable noise estimation with random unitary operators, *Journal of Optics B: Quantum and Semiclassical Optics* **7**, S347 (2005).
- [25] A. Morvan, V. V. Ramasesh, M. S. Blok, J. M. Kreikebaum, K. O’Brien, L. Chen, B. K. Mitchell, R. K. Naik, D. I. Santiago, and I. Siddiqi, Qutrit randomized benchmarking, *Phys. Rev. Lett.* **126**, 210504 (2021).
- [26] M. Kononenko, M. A. Yurtalan, S. Ren, J. Shi, S. Ashhab, and A. Lupascu, Characterization of control in a superconducting qutrit using randomized benchmarking, *Phys. Rev. Research* **3**, L042007 (2021).
- [27] R. Blume-Kohout, J. K. Gamble, E. Nielsen, K. Rudinger, J. Mizrahi, K. Fortier, and P. Maunz, Demonstration of qubit operations below a rigorous fault tolerance threshold with gate set tomography, *Nature Communications* **8**, 14485 (2017).
- [28] K. Temme, S. Bravyi, and J. M. Gambetta, Error mitigation for short-depth quantum circuits, *Phys. Rev. Lett.* **119**, 180509 (2017).
- [29] S. Endo, S. C. Benjamin, and Y. Li, Practical quantum error mitigation for near-future applications, *Phys. Rev. X* **8**, 031027 (2018).
- [30] L. F. Gladden, Process tomography: Principles, techniques and applications, *Measurement Science and Technology* **8**, 10.1088/0957-0233/8/4/021 (1997).
- [31] D. Greenbaum, *Introduction to Quantum Gate Set Tomography*, (2015).
- [32] E. Nielsen, J. K. Gamble, K. Rudinger, T. Scholten, K. Young, and R. Blume-Kohout, Gate set tomography, *Quantum* **5**, 557 (2021).
- [33] A. Ash-Saki, M. Alam, and S. Ghosh, Experimental characterization, modeling, and analysis of crosstalk in a quantum computer, *IEEE Transactions on Quantum Engineering* **1**, 1 (2020).
- [34] T. Proctor, K. Rudinger, K. Young, E. Nielsen, and R. Blume-Kohout, Measuring the capabilities of quan-

- tum computers, *Nature Physics* **18**, 75 (2022).
- [35] G. A. L. White, C. D. Hill, F. A. Pollock, L. C. L. Hollenberg, and K. Modi, Demonstration of non-markovian process characterisation and control on a quantum processor, *Nature Communications* **11**, 6301 (2020).
- [36] S. Ma, A. P. Burgers, G. Liu, J. Wilson, B. Zhang, and J. D. Thompson, Universal gate operations on nuclear spin qubits in an optical tweezer array of  $^{171}\text{Yb}$  atoms (2021).
- [37] G. White, C. Hill, and L. Hollenberg, Performance optimization for drift-robust fidelity improvement of two-qubit gates, *Phys. Rev. Applied* **15**, 014023 (2021).
- [38] T. Proctor, M. Reville, E. Nielsen, K. Rudinger, D. Lobser, P. Maunz, R. Blume-Kohout, and K. Young, Detecting and tracking drift in quantum information processors, *Nature Communications* **11**, 5396 (2020).
- [39] J. Rahamim, T. Behrle, M. J. Peterer, A. Patterson, P. A. Spring, T. Tsunoda, R. Manenti, G. Tancredi, and P. J. Leek, Double-sided coaxial circuit qed with out-of-plane wiring, *Applied Physics Letters* **110**, 222602 (2017).
- [40] P. A. Spring, S. Cao, T. Tsunoda, G. Campanaro, S. Fasciati, J. Wills, M. Bakr, V. Chidambaram, B. Shteynas, L. Carpenter, P. Gow, J. Gates, B. Vlastakis, and P. J. Leek, High coherence and low cross-talk in a tileable 3d integrated superconducting circuit architecture, *Science Advances* **8**, eabl6698 (2022).
- [41] D. C. McKay, C. J. Wood, S. Sheldon, J. M. Chow, and J. M. Gambetta, Efficient  $z$  gates for quantum computing, *Phys. Rev. A* **96**, 022330 (2017).
- [42] M. Bydder, A. Rahal, G. D. Fullerton, and G. M. Bydder, The magic angle effect: A source of artifact, determinant of image contrast, and technique for imaging, *Journal of Magnetic Resonance Imaging* **25**, 290 (2007).
- [43] A. Y. Kitaev, A. H. Shen, and M. N. Vyalyi, *Classical and Quantum Computation* (American Mathematical Society, USA, 2002).
- [44] E. Nielsen, J. K. Gamble, K. Rudinger, T. Scholten, K. Young, and R. Blume-Kohout, Gate Set Tomography, *Quantum* **5**, 557 (2021).
- [45] E. Nielsen, K. Rudinger, T. Proctor, A. Russo, K. Young, and R. Blume-Kohout, Probing quantum processor performance with pyGSTi, *Quantum Science and Technology* **5**, 044002 (2020).
- [46] J. J. Moré, The levenberg-marquardt algorithm: Implementation and theory, in *Numerical Analysis*, edited by G. A. Watson (Springer Berlin Heidelberg, Berlin, Heidelberg, 1978) pp. 105–116.
- [47] M. A. Yurtalan, J. Shi, M. Kononenko, A. Lupascu, and S. Ashhab, Implementation of a walsh-hadamard gate in a superconducting qutrit, *Phys. Rev. Lett.* **125**, 180504 (2020).
- [48] R. Bianchetti, S. Filipp, M. Baur, J. M. Fink, C. Lang, L. Steffen, M. Boissonneault, A. Blais, and A. Wallraff, Control and tomography of a three level superconducting artificial atom, *Phys. Rev. Lett.* **105**, 223601 (2010).
- [49] Each measurement obtains the probability of 3 different states, however, because they always sum up to be 1, so each measurement can only remove maximum 2 degrees of freedom.
- [50] R. Blume-Kohout, M. P. da Silva, E. Nielsen, T. Proctor, K. Rudinger, M. Sarovar, and K. Young, A taxonomy of small markovian errors, *PRX Quantum* **3**, 020335 (2022).
- [51] E. Magesan, J. M. Gambetta, B. R. Johnson, C. A. Ryan, J. M. Chow, S. T. Merkel, M. P. da Silva, G. A. Keefe, M. B. Rothwell, T. A. Ohki, M. B. Ketchen, and M. Steffen, Efficient measurement of quantum gate error by interleaved randomized benchmarking, *Phys. Rev. Lett.* **109**, 080505 (2012).
- [52] F. Motzoi, J. M. Gambetta, P. Rebentrost, and F. K. Wilhelm, Simple pulses for elimination of leakage in weakly nonlinear qubits, *Phys. Rev. Lett.* **103**, 110501 (2009).
- [53] The definition is from the PyGSTi source code.

---

## Appendix A: Hardware details

The basic characterization result of the device is shown in Table III. The physical single qutrit gate is implemented with 30 nanoseconds microwave pulses with DRAG correction [52] and Blackman window. The control pulses RF signal is mixed with a IF signal generated by a 2 Gsps DAC and a fixed LO signal. To cover the transition frequency of the  $\{|0\rangle, |1\rangle\}$ ,  $\{|1\rangle, |2\rangle\}$  and  $\{|2\rangle, |3\rangle\}$ , the LO frequency is chosen to be 3.904 GHz, which causes the IF frequency of  $\{|0\rangle, |1\rangle\}$  transition to be 230 MHz. 230 MHz is at the very edge of our DAC's operatable frequency range. We suggest that this can be the cause of the finding that the gates in the  $\{|0\rangle, |1\rangle\}$  subspace have lower fidelities than those in the  $\{|1\rangle, |2\rangle\}$  subspace.

## Appendix B: PTM and Gellman matrices

The superoperator formalism represents a density matrix  $\rho$  as a vector (superket)  $|\rho\rangle\rangle = \sum_m |m\rangle\rangle\langle\langle m|\rho\rangle\rangle$  in a Hilbert-Schmidt space with dimension  $d^2$ , where  $|m\rangle\rangle$  is the unit vector along each basis and  $d$  is the dimension of the quantum system. The inner product in the Hilbert-Schmidt space is defined as  $\langle\langle\rho_A|\rho_B\rangle\rangle = \text{Tr}(\rho_A\rho_B^\dagger)/d$ , where  $\rho_A$  and  $\rho_B$  are density operators. In this representation, quantum operations can be represented as Pauli transfer matrix (PTM)  $R_A = \sum_{m,n} |m\rangle\rangle\langle\langle m|R_A|n\rangle\rangle\langle\langle n|$  with dimension  $d^2 \times d^2$ . The  $ij$  element of the PTM can be calculated from,

$$(R_A)_{ij} = \frac{1}{d} \text{Tr}\{P_i \Lambda(P_j)\}. \quad (\text{B1})$$

Subspace	Parameter		Value
	Resonator frequency	$f_{Res}$ (MHz)	8783
$ 0\rangle,  1\rangle$	Transition frequency	$f_{01}$ (MHz)	4134.33
$ 0\rangle,  1\rangle$	Relaxation time	$T_1^{(01)}$ (us)	$221 \pm 30$
$ 0\rangle,  1\rangle$	Hahn decoherence time	$T_2^{(01)}$ Echo (us)	$126 \pm 15$
$ 0\rangle,  1\rangle$	Ramsey decoherence time	$T_2^{(01)}$ Ramsey (us)	$96 \pm 10$
$ 1\rangle,  2\rangle$	Transition frequency	$f_{12}$ (MHz)	3937.66
$ 1\rangle,  2\rangle$	Relaxation time	$T_1^{(12)}$ (us)	$119 \pm 20$
$ 1\rangle,  2\rangle$	Hahn decoherence time	$T_2^{(12)}$ Echo (us)	$76 \pm 27$
$ 1\rangle,  2\rangle$	Ramsey decoherence time	$T_2^{(12)}$ Ramsey (us)	$52 \pm 4$

TABLE III. Summary of device parameters

The  $(R_\Lambda)_{ij}$  denote the expectation value when the state is prepared in the  $P_j$  basis, and measured in the  $P_i$  basis after applying the quantum process. The PTM conveniently acts on the state like

$$R_\Lambda|\rho\rangle\rangle = |\Lambda(\rho)\rangle\rangle, \quad (\text{B2})$$

where  $\Lambda$  denotes the quantum channel  $\Lambda(\rho) = \sum_{i=1}^N K_i \rho K_i^\dagger$  and  $K_i$  are Kraus operators. Furthermore, two quantum operations on a quantum map can just be seen as applying one PTM to the state after the other

$$R_{\Lambda_1 \cdot \Lambda_2}|\rho\rangle\rangle = R_{\Lambda_1}R_{\Lambda_2}|\rho\rangle\rangle = |\Lambda_2(\Lambda_1(\rho))\rangle\rangle. \quad (\text{B3})$$

The above discussion is valid for system with arbitrary dimensions, and any basis  $|m\rangle\rangle$  can be used in the Hilbert-Schmidt space. However it is useful to define a basis that is orthonormal, hermitian, and traceless for all members in the basis apart from the identity. For the 3-level system demonstrated in this letter, we chose the Gell-Mann matrices and the qutrit identity as the basis operators, which naturally generalise the qubit Pauli basis are orthonormal, hermitian, and traceless:

$$\begin{aligned}
I &= \begin{pmatrix} 1 & 0 & 0 \\ 0 & 1 & 0 \\ 0 & 0 & 1 \end{pmatrix} & X_{01} &= \begin{pmatrix} 0 & 1 & 0 \\ 1 & 0 & 0 \\ 0 & 0 & 0 \end{pmatrix} & X_{02} &= \begin{pmatrix} 0 & 0 & 1 \\ 0 & 0 & 0 \\ 1 & 0 & 0 \end{pmatrix} \\
X_{12} &= \begin{pmatrix} 0 & 0 & 0 \\ 0 & 0 & 1 \\ 0 & 1 & 0 \end{pmatrix} & Y_{01} &= \begin{pmatrix} 0 & -i & 0 \\ i & 0 & 0 \\ 0 & 0 & 0 \end{pmatrix} & Y_{02} &= \begin{pmatrix} 0 & 0 & -i \\ 0 & 0 & 0 \\ i & 0 & 0 \end{pmatrix} \\
Y_{12} &= \begin{pmatrix} 0 & 0 & 0 \\ 0 & 0 & -i \\ 0 & i & 0 \end{pmatrix} & Z_1 &= \begin{pmatrix} 1 & 0 & 0 \\ 0 & -1 & 0 \\ 0 & 0 & 0 \end{pmatrix} & Z_2 &= \frac{1}{\sqrt{3}} \begin{pmatrix} 1 & 0 & 0 \\ 0 & 1 & 0 \\ 0 & 0 & -2 \end{pmatrix}
\end{aligned} \quad (\text{B4})$$

With the basis defined above, we present the reconstructed PTM and post-gate error generators for all parametrized gate in the gate set in Figure 6.

### Appendix C: Projected error generators

The error generator  $L$  describes the full error information of the reconstructed gate PTM.  $L$  can be decomposed into *elementary generators*, where each element has a recognizable interpretation [50]. The decomposition of  $L$  is given by

$$\begin{aligned}
L &= L_{\mathcal{H}} + L_S + L_C + L_A \\
&= \sum_P h_P H_P + \sum_P s_P S_P + \sum_{P,Q>P} c_{P,Q} C_{P,Q} + \sum_{P,Q>P} a_{P,Q} A_{P,Q}
\end{aligned} \quad (\text{C1})$$

where

$$H_P[\rho] = -i[P, \rho] \quad (\text{C2})$$

$$S_P[\rho] = P\rho P - I\rho I \quad (\text{C3})$$

$$C_{P,Q}[\rho] = P\rho Q + Q\rho P - \frac{1}{2}\{\{P, Q\}, \rho\} \quad (\text{C4})$$

$$A_{P,Q}[\rho] = i(P\rho Q - Q\rho P + \frac{1}{2}\{\{P, Q\}, \rho\}) \quad (\text{C5})$$

$H_P$  is the Hamiltonian projected error generator,  $S_P$  and  $C_{P,Q}$  is the Pauli and Pauli-correlated projected stochastic error generator and  $A_{P,Q}$  is the active projected error generator.  $P$  and  $Q$  are distinct basis, which usually chosen to be Pauli matrices for qubits, and in this work we use Gellman matrices as discussed in appendix B. The  $H_P$  describes all the coherent errors. The Hamiltonian projected power of the Hamiltonian error  $p_{\mathcal{H}}$  quantifies the ratio of the coherent error, given by [53]

$$p_{\mathcal{H}} = \frac{\|L_{\mathcal{H}}\|}{\|L_{\mathcal{H}}\| + \|L_{\mathcal{S}}\| + \|L_{\mathcal{C}}\| + \|L_{\mathcal{A}}\|} \quad (\text{C6})$$

where  $\|X\| = (\sum_{i,j} x_{ij}^2)^{\frac{1}{2}}$  is the entry-wise 2-norm of the matrix  $X$ .

---

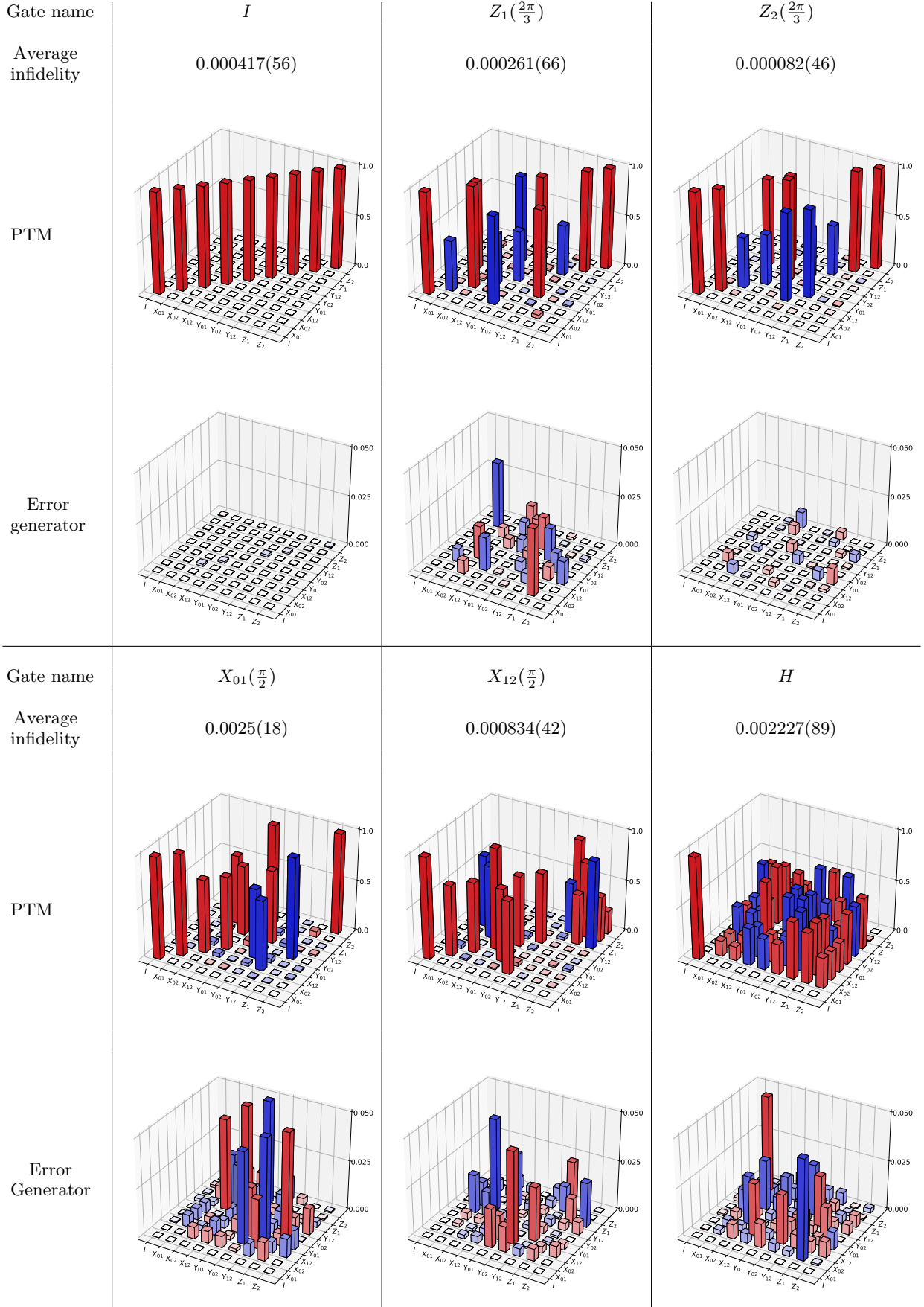


FIG. 6. Averaged gate infidelities, reconstructed process matrix and error generators of the gate set. The result is generated by pyGSTi maximum likelihood estimation.